Lawrence Berkeley National Laboratory
LBL Publications

## Title

Direct Measurement of the Thermal Expansion Coefficient of Epitaxial WSe2 by Four-Dimensional Scanning Transmission Electron Microscopy.

## Permalink

https://escholarship.org/uc/item/8qb0q2fr

## Journal

ACS Nano, 18(27)

## Authors

Kucinski, Theresa
Dhall, Rohan
Savitzky, Benjamin
et al.

## Publication Date

2024-07-09

## DOI

10.1021/acsnano.4c02996

Peer reviewed

eScholarship.org Powered by the California Digital Library
University of California

ACS NANO

www.acsnano.org

Open Access

This article is licensed under CC-BY-NC-ND 4.0

ARTICLE

# Direct Measurement of the Thermal Expansion Coefficient of Epitaxial $WSe_2$ by Four-Dimensional Scanning Transmission Electron Microscopy

Theresa M. Kucinski, Rohan Dhall, Benjamin H. Savitzky, Colin Ophus, Rijan Karkee, Avanish Mishra, Enkeleda Dervishi, Jung Hoon Kang, Chul-Ho Lee, Jinkyoung Yoo, and Michael T. Pettes*

Cite This: *ACS Nano* 2024, 18, 17725−17734

Read Online

ACCESS | Metrics & More | Article Recommendations | Supporting Information

**ABSTRACT:** **Current reports of thermal expansion coefficients (TEC) of two-dimensional (2D) materials show large discrepancies that span orders of magnitude. Determining the TEC of any 2D material remains difficult due to approaches involving indirect measurement of samples that are atomically thin and optically transparent. We demonstrate a methodology to address this discrepancy and directly measure TEC of nominally monolayer epitaxial $WSe_2$ using four-dimensional scanning transmission electron microscopy (4D-STEM). Experimentally, $WSe_2$ from metal−organic chemical vapor deposition (MOCVD) was heated through a temperature range of 18−564 °C using a barrel-style heating sample holder to observe temperature-induced structural changes without additional alterations or destruction of the sample. By combining 4D-STEM measurements with quantitative structural analysis, the thermal expansion coefficient of nominally monolayer polycrystalline epitaxial 2D $WSe_2$ was determined to be $(3.5 \pm 0.9) \times 10^{-6}$ $K^{-1}$ and $(5.7 \pm 2) \times 10^{-5}$ $K^{-1}$ for the in- and out-of-plane TEC, respectively, and $(3.6 \pm 0.2) \times 10^{-5}$ $K^{-1}$ for the unit cell volume TEC, in good agreement with historically determined values for bulk crystals.**

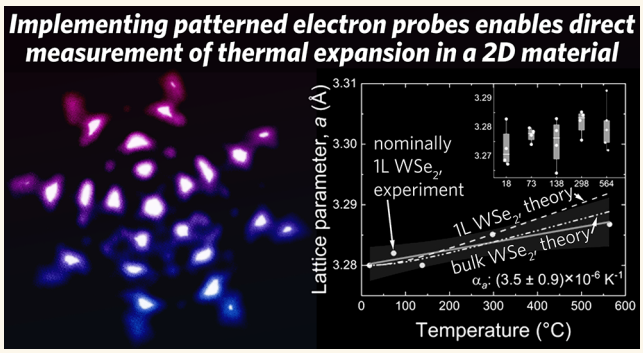


**KEYWORDS:** *thermal expansion, 2D materials, 4D-STEM, MOCVD, orientation, strain*

Microelectronics has been a transformative technology but is now facing technical challenges that require the use of advanced materials and architectures, of which two-dimensional (2D) materials with hexagonal crystal structures are being considered as constituents of both three-dimensional heterogeneous architectures and as compliant intralayers for the growth of group-III nitrides; in all instances of their possible integration in future technologies, the strain and thermal stress distributions in 2D materials remains a critical metrology challenge.[1] This challenge is mainly driven by the issue of thermal expansion mismatch in constituent materials, and this physical property is not well understood in the family of hexagonal 2D transition metal dichalcogenides (TMDs) leading to conflicting reports that differ by an order of magnitude.[2,3] Innovations in microelectronic applications such as materials, fabrication processes, and characterization methods are required to continue innovation in this application area, where next-generation devices can benefit from 2D semiconducting materials' electronic, optical, mechanical, and thermal properties.[4−17] These include materials such as the layered TMDs, which are maturing toward nanophotonic and quantum device applications.[1,18−25] Operation of such devices generates heat, thermal processing can impart large residual stress, and recent ways in which both process-induced and tunable-strain[26−28] are being applied to modify electron mobility all bring challenges related to the need for strain and thermal stress metrology; however, understanding of thermomechanical properties of 2D TMDs remains insufficient to fully under-

Received: March 4, 2024
Revised: June 3, 2024
Accepted: June 12, 2024
Published: June 27, 2024

ACS Publications

© 2024 The Authors. Published by American Chemical Society

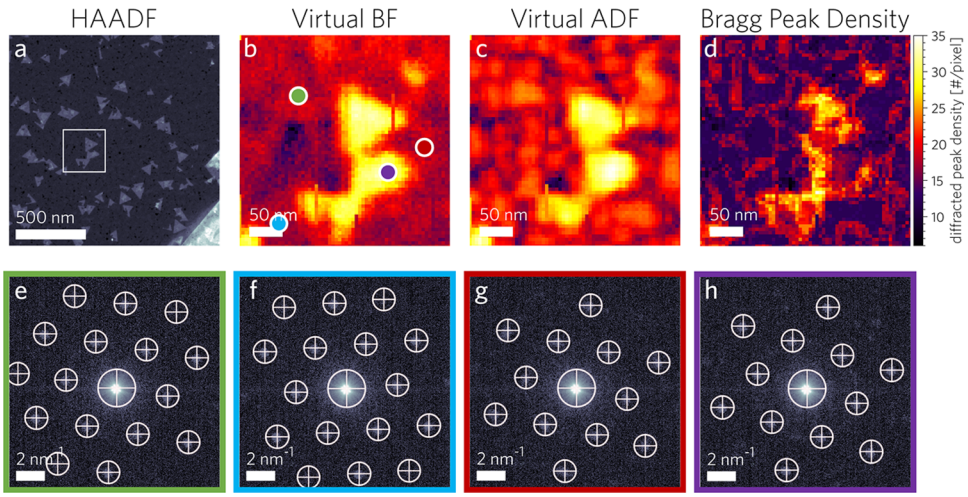


**Figure 1. (a) Plan-view HAADF-STEM of the polycrystalline monolayer $WSe_2$ film showing a white box to denote the 4D-STEM data acquisition region for sample 1. Triangular islands on top of the film are from bilayer overgrowths. (b) Virtual bright-field image (BF, inverse intensity), (c) virtual annular dark-field image (ADF), and (d) Bragg peak density image reconstructed from the 4D-STEM data set. Filled colored circles in (b) correspond to NBED patterns (e−h) collected at the corresponding real space location, with detected peak locations depicted by circled crosses.**

stand and predict heat-related performance issues. Proper investigation into thermal properties, such as the thermal expansion coefficient (TEC), has not been fully realized due to insufficient local characterization techniques, which are complicated by the atomically thin nature of 2D TMDs.

Monolayer 2D materials have been predicted to display nonintuitive thermal expansion behaviors, with indication from experiments reported in 1960.[29] Discussion of the TEC in monolayer 2D materials continues in the present due to behavior that may differ from their bulk counterparts, such as negative TEC values reported for graphene,[29,30] and few-layer $MoS_2$ at temperatures below 175 K,[31] which may vary in the room-temperature-and-above regime relevant to many technological applications.

Lab-scale demonstrations of high-performance 2D TMD-based devices often rely on exfoliation from high-quality bulk crystals; however, this procedure is both inadequate at the industrial scale and not representative of materials synthesized from industrially relevant processes. Other synthesis methods, including metal−organic chemical vapor deposition (MOCVD), have greater applicability for microelectronics,[32−34] where they can be used in large-area batch fabrication.[35−37] Understanding the thermal behavior of 2D TMDs fabricated from MOCVD is thus critical for understanding how the material will behave in real application settings under thermal loads. For example, controlled strain engineering utilizing thermal mismatch with a substrate can further enhance electronic and mechanical properties.[23,38,39] Furthermore, thermal management design considerations are critical for future 2D TMD-based devices because localized heat generation can lead to device degradation or delamination.[40]

Lack of spatial resolution in common temperature measurements and inconsistency in nanoscale thermometry have limited the characterization of thermomechanical properties for 2D TMDs. Several techniques have been proposed to address these inconsistencies and include Raman spectroscopy, synchrotron scattering, electron energy loss spectroscopy (EELS), transmission electron microscopy (TEM), and atomic force microscopy (AFM).[2,31,41−44] In these techniques, thermal measurements are often indirect measurements of a temperature-dependent phenomenon or rely on a substrate which introduces strong effects that may ultimately be neglected in measurements.[45] Reported TECs are inconsistent across techniques and can range from several orders of magnitude. For instance, the in-plane TEC for $WSe_2$ has been reported from $10^{-5}$ to $10^{-6}$ $K^{-1}$.[2,3,46,47] The uncertainty surrounding experimental TECs remains unresolved, which limits the optimization of 2D TMD materials for microelectronic development.

Here, we present a substrate-free experimental characterization technique to directly measure the localized thermal expansion coefficient of the polycrystalline 2D TMD material $WSe_2$, using 4-dimensional scanning transmission electron microscopy (4D-STEM)[48−50] paired with complex computational data analysis. 4D-STEM enables the fast collection of convergent-beam/nanobeam electron diffraction (CBED/NBED) patterns over a 2D array of electron beam raster positions, resulting in a data set composed of many 2D diffraction patterns, one at each real (sample) space pixel location. Because the illumination is highly localized, these diffraction patterns probe the local sample structure. The probe size full width at half-maximum (FWHM) is ∼14 nm in the experimental configuration used here. Computational analysis of the collection of diffraction patterns reveal structural variations occurring within the $WSe_2$ sample upon heating.[51] Our method overcomes the challenges of substrate effects, indirect measurements, and spatial resolution to accurately determine the localized TECs of a 2D TMD material using electron diffraction patterns.

## RESULTS AND DISCUSSION

The data resulting from a 4D-STEM experiment require processing prior to analysis. We first determined the positions of Bragg disk reflections, which correspond to the reciprocal lattice points, in each diffraction pattern (Figure 1). The recorded image of the patterned probe over a vacuum in diffraction space (Figure S1, Supporting Information) was used to create a matching template. The template was then used to detect signal positions in the diffraction patterns by computing


https://doi.org/10.1021/acsnano.4c02996
ACS Nano 2024, 18, 17725−17734

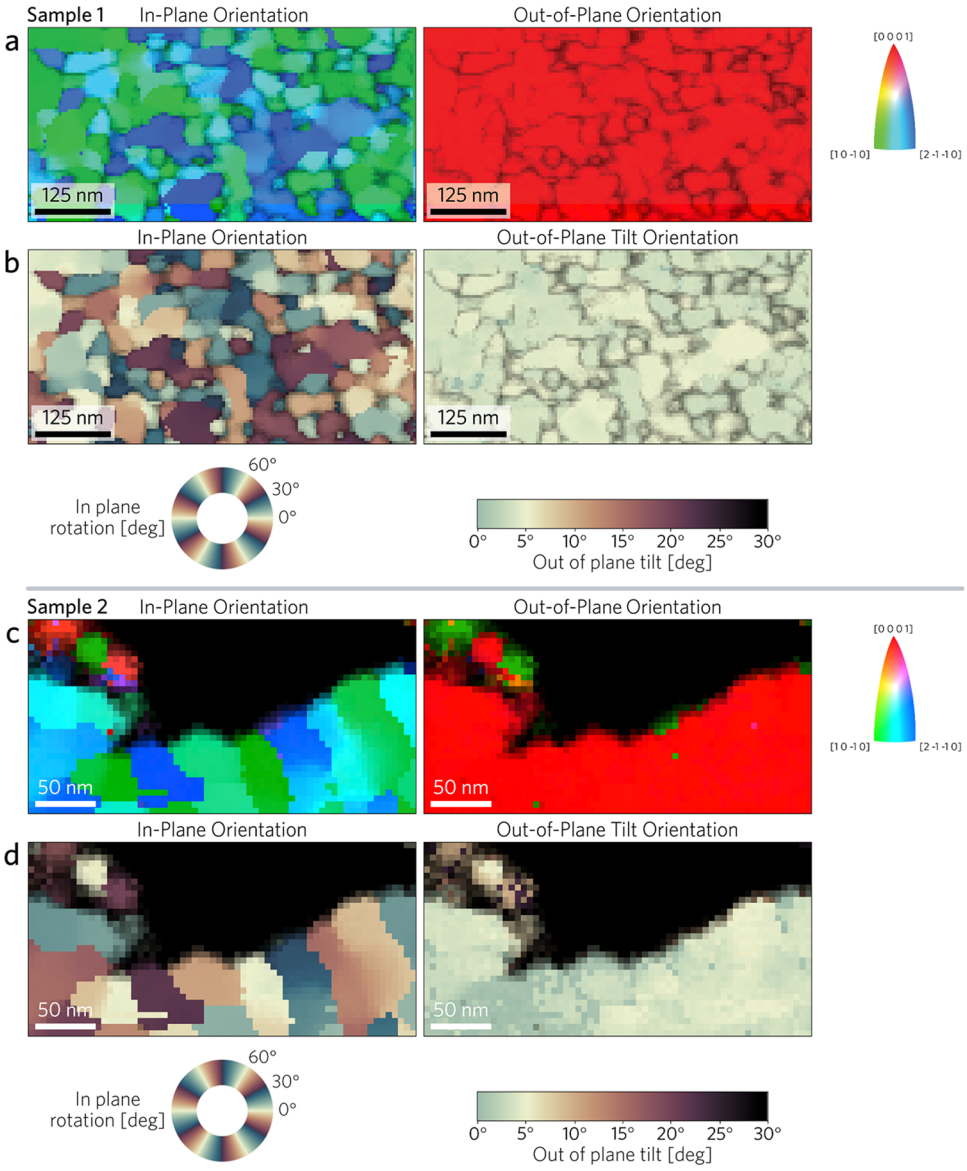


**Figure 2. Automated crystal orientation mapping analysis for $WSe_2$ samples 1 (a, b) and 2 (c, d). (a, c) In-plane and out-of-plane orientation maps indexed to principal symmetry directions. (b, d) In-plane rotation about the [0001] zone axis with respect to the [10$\bar{1}$0] in-plane direction and out-of-plane tilt relative to the [0001] zone axis.**

cross-correlations then locating the correlation maxima. A patterned probe[52] was created using an aperture with an etched pattern in the electron beam condenser system, allowing for more precise detection due to matching of the additional pattern features in each Bragg disk reflection. The detected Bragg disk reflections for each scan position (Figure 1e–h) are stored for subsequent statistical analysis.

The detected Bragg disk reflections are collapsed into a Bragg vector map, defined as a 2D histogram of measured Bragg vector locations and intensities describing the reciprocal lattice vector distribution in the sample over the full 4D-STEM scan area (Figure S2, Supporting Information). Precise measurements of the reciprocal lattice vectors can then be measured that are inversely proportional to the real space atomic spacing in the sample (individual indexed nanodiffraction patterns are shown in Figure S3, Supporting Information). In any 4D-STEM data set, distortions are unavoidable and must be corrected for accurate quantitative analysis. Elliptical distortions result from imperfect alignments and lens distortions which can significantly impact measurement accuracy even in well-aligned systems but can be corrected within the precision of the measurement.[53] We corrected elliptical distortions in our data sets by applying an annular region fit to the uncalibrated data (Figure S2, Supporting Information). Elliptical correction for these data was on the order of 3%. Pattern shifts were corrected by locating the deviation of the center beam. The localized and calibrated Bragg vectors were then used to extract the structural parameters and orientation.

Figure 2 presents the results of computational analysis to gain insights into the evolution of orientation and strain as a function of temperature that was performed using py4DSTEM with automated crystal orientation mapping (ACOM).[48,49,54] ACOM produces orientation and strain maps from 4D-STEM data sets by using a fast sparse correlation procedure which determines the orientation of each diffraction pattern. For $WSe_2$, we determined the in-plane and out-of-plane orienta-



https://doi.org/10.1021/acsnano.4c02996
ACS Nano 2024, 18, 17725−17734

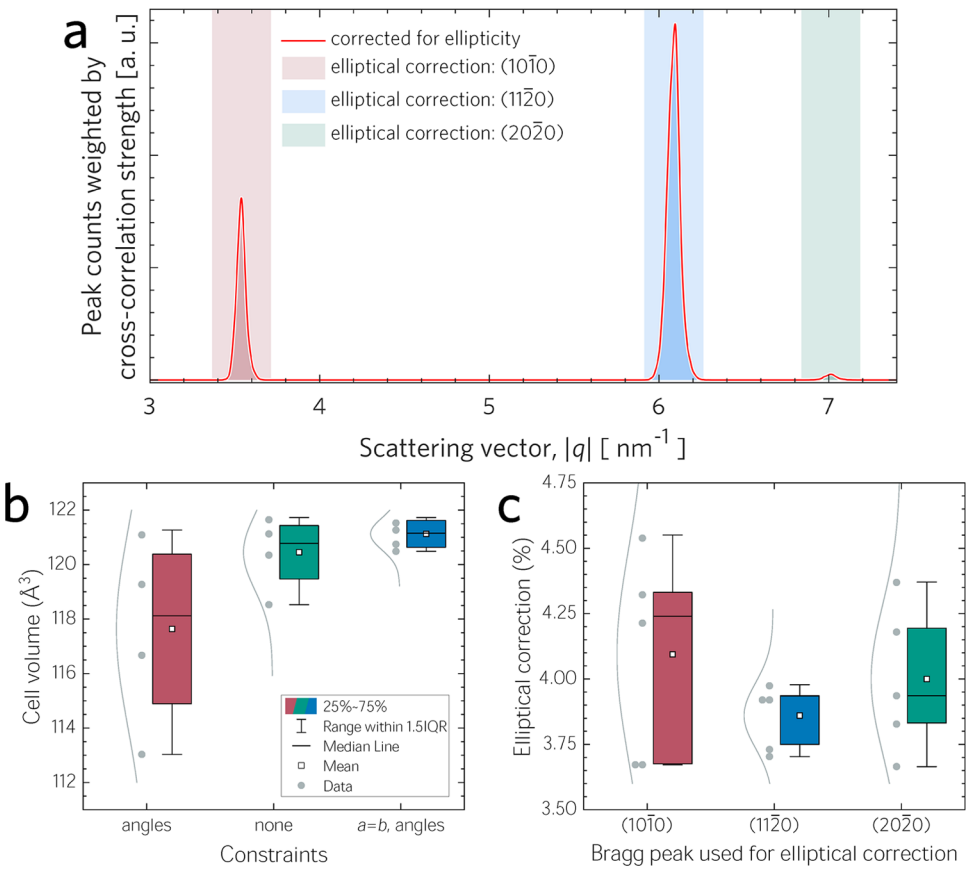


**Figure 3. (a) Radial histogram of detected Bragg peaks; the red line corresponds to the elliptically corrected data. Specific Bragg peaks used during the elliptical correction and subsequent computational analyses are shown as colored bands: (10$\bar{1}$0) red, (11$\bar{2}$0) blue, and (20$\bar{2}$0) green. (b) Calculated unit cell volume as a function of computational constraints for fitting lattice parameters *a*, *b*, *c*, *α*, *β*, and *γ*. "angles" indicates constraints of *α* = *β* = 90° and *γ* = 120°. (c) Comparison of the amount of elliptical distortion corrected for by fitting different Bragg peaks during the computational analysis. Distribution of resulting data (b, c) shows the optimal peak selection is obtained using (11$\bar{2}$0) with *a* = *b* and fixed angles.**

tions for both samples, which are displayed with rotation visually represented by a colormap.

Three Bragg peaks were present in the experimental configuration used to measure the $WSe_2$ samples corresponding to the rings in the Bragg vector map and the peaks in the radial peak histogram (Figure 3a). The peaks corresponded to the (10$\bar{1}$0), (11$\bar{2}$0), and (20$\bar{2}$0) crystal planes. Sample 2 was torn, which created a roll edge producing a small peak corresponding to (01$\bar{1}$1) from the variation of orientation which was not seen in sample 1 (Figure 2c,d). We were thus able to measure the TEC along the *c*-axis direction by utilizing the (01$\bar{1}$1) peak in sample 2. Figure 3 and Table 1 present a comparison between several fitting methods to illustrate the significance of the calibration and data analysis methodology used to obtain crystallographic information.

Figure 3b shows the calculated cell volume for each of the several measurements collected at 18 °C under computational constraints and under constraint-free conditions. Figure 3c shows the elliptical distortion correction required for all of the scans performed at 18 °C as a function of fitting to the three different Bragg peaks. Table 1 compares the cell volume difference, full width at half-maximum (FWHM), and elliptical correction for each measurement at 18 °C calculated for the three different peak fits. Two scans were collected for sample 1 under different beam stop conditions. Cell volume difference was calculated using the computed cell volume and the $WSe_2$

**Table 1. Results for $WSe_2$ at 18 °C under No Beam Stop and Beam Stop Conditions for both Samples Using Each of the Three Peaks (10$\bar{1}$0), (11$\bar{2}$0), and (20$\bar{2}$0) for Elliptical Distortion Correction[a]**

| | No Beam Stop | | Beam Stop | | |
|---|---|---|---|---|---|
| **Sample** | 1 | 2 | 1(a) | 1(b) | 2 |
| **Peak** | **(10$\bar{1}$0)** | | | | |
| **Cell Volume Difference (%)** | 10.13 | 0.31 | 4.08 | 10.13 | 1.93 |
| **FWHM (11$\bar{2}$0) (Å$^{-1}$)** | 0.62 | 0.62 | 1.11 | 0.73 | 0.58 |
| **Elliptical Correction (%)** | 4.19 | 3.67 | 4.37 | 3.94 | 3.83 |
| **Peak** | **(11$\bar{2}$0)** | | | | |
| **Cell Volume Difference (%)** | 0.10 | 0.27 | 0.83 | 0.75 | 0.50 |
| **FWHM (11$\bar{2}$0) (Å$^{-1}$)** | 0.21 | 0.20 | 0.40 | 0.19 | 0.18 |
| **Elliptical Correction (%)** | 3.98 | 3.70 | 3.93 | 3.94 | 3.75 |
| **Peak** | **(20$\bar{2}$0)** | | | | |
| **Cell Volume Difference (%)** | 0.72 | 0.16 | 0.83 | 0.18 | 0.73 |
| **FWHM (11$\bar{2}$0) (Å$^{-1}$)** | 0.17 | 0.16 | 0.29 | 0.15 | 0.17 |
| **Elliptical Correction (%)** | 4.33 | 3.67 | 4.55 | 4.24 | 3.68 |

[a]Unit cell volume difference from expected value (%), the FWHM of the 11$\bar{2}$0 peak after correction by the three fitting profiles, and the elliptical correction (%). These results indicate that fitting the 11$\bar{2}$0 peak is most optimal for corrections. The comparison also indicates no statistical difference for no beam stop and beam stop conditions as well as scanning sample location in the polycrystalline epitaxial film.



https://doi.org/10.1021/acsnano.4c02996
ACS Nano 2024, 18, 17725−17734

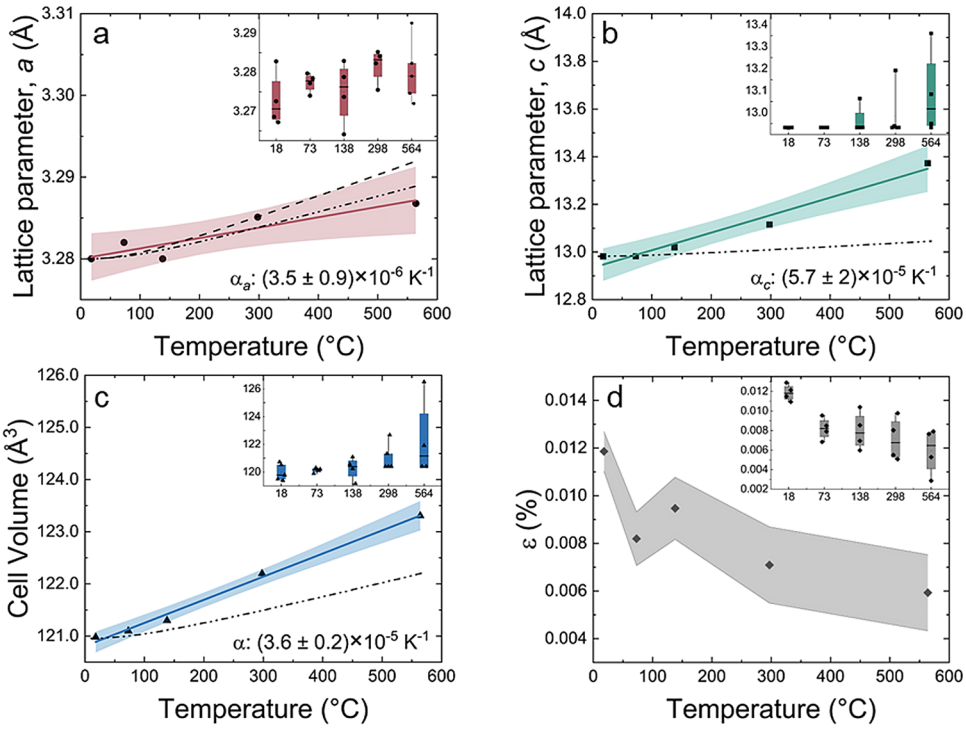


**Figure 4. (a) *a* = *b*- and (b) *c*-lattice parameters, (c) unit cell volume, and (d) apparent microstrain as a function of temperature. Shaded regions indicate the 95% confidence bands. (a−c) *Ab initio* calculated values are shown for monolayer (dashed line) and bulk (dash-dot-dot line) $WSe_2$. The measured (a) in-plane and (b) out-of-plane thermal expansion coefficients for $WSe_2$ are (3.5 ± 0.9) × 10$^{-6}$ K$^{-1}$ and (5.7 ± 2) × 10$^{-5}$ K$^{-1}$, respectively, which are in good agreement with reported experimental bulk values. The cell volume TEC is (3.6 ± 0.2) × 10$^{-5}$ K$^{-1}$. The out-of-plane fit (b) only included sample 2 data due to the presence of (01$\bar{1}$0) peaks from the rolled edge near a fracture. Apparent microstrain represents the quantification of the upper limit of strain in the sample obtained through full peak-profile analysis and shows an overall decrease with increasing temperature.**

cell volume from powder diffraction file 00-038-1388.[55] FWHMs for the 11$\bar{2}$0 peak in reciprocal space and the elliptical distortion correction (%) were compared for each measurement at 18 °C. Elliptical corrections at 18 °C for the beam stop and no beam stop conditions from fitting the 11$\bar{2}$0 peak were used for the increased temperature measurements.

We show that the analysis is dependent on which crystal orientation peak is used in the calibration fitting and is an important consideration in this analysis methodology. Comparison of the elliptical correction (Figure 3b) indicates that fitting to the (11$\bar{2}$0) peak produces the smallest mean value with the lowest spread, which is in good agreement with the calculated cell volume difference from the expected value (Table 1). When calculating the lattice parameters, additional fitting methods need to be considered. In the calculation, in-plane lattice parameters can be locked to the same value, which can be beneficial in the case of hexagonal structures, which stipulates that *a* and *b* lattice constants must be equal. Another option is to lock angles to known inputted values that reflect the qualities of the crystal structure. $WSe_2$ is known to be hexagonal and defining the calculation to locking *a* = *b* as well as the angles $\alpha = \beta = 90°$, and $\gamma = 120°$ produced the most precise value for cell volume (Figure 3c), corresponding to the assumption that changes occurring in the lattice during our measurements are isotropic in-plane and preserve the symmetry of the hexagonal unit cell. Results from quantitative analysis show a dependence on the fitting of peak profiles.

Statistical analyses, including the *t*-test and analysis of variance (ANOVA), were performed on the data sets to compare experimental methods. We found no statistically significant difference between the experimental conditions of implementing a beam stop before the Gatan Orius 830 camera and not implementing one, which is reflected in the data in Table 1. Additionally, a partial fracture was present in the scanning range of sample 2 that captured changes in the lattice parameter *c* due to the rolled edge but otherwise did not reflect any meaningful changes within the data. Extensive uncertainty analysis reveals that computational parameters including peak fitting parameters can influence the precision in capturing local lattice parameters. Our comparison of the fitting parameters used in the computational methods indicates that proper calibration is a priority, and extra care must be given to determining the analysis route to ensure precision and accuracy.

Several measurements of the samples were collected at five temperatures ranging from 18 to 564 °C, and statistics of our measurements as a function of temperature are shown in Figure 4. In the main panels, best fit lines are presented with their 95% confidence interval shown as shaded bands, showing the limits of all possible fitted lines for the data. Linear TECs were calculated from the slope of the lines using all datapoints from each 4D-STEM scan (Figure 4a−c). The insets display the distributions of the individual datapoints. Each temperature position contains measurements from four to six 4D-STEM acquisitions, each containing ∼8192 diffraction images. The boxes show the 25th to 75th percentiles for all diffraction images obtained at a given temperature, the mean is indicated by the solid line, and the whiskers show the fifth and 95th percentiles. We used the slope from the plots of lattice parameters as a function of the temperature to calculate the


https://doi.org/10.1021/acsnano.4c02996
ACS Nano 2024, 18, 17725−17734

linear TEC. ANOVA indicates that the slope used to calculate the TEC is significantly different from zero for all parameters at the 0.05 confidence level for all temperature-dependent fits.

As shown in Figure 4, the lattice parameters produced from the analysis were used to calculate the thermal expansion coefficients of $WSe_2$. We measured the in-plane thermal expansion coefficient for $WSe_2$ as $(3.5 \pm 0.9) \times 10^{-6}$ $K^{-1}$ (Figure 4a) which is in good agreement with the expected bulk values.[44,56,57] Other common semiconductors within the same range ($10^{-6}$ $K^{-1}$) further support the results from this methodology and show potential for material compatibility with industrially relevant semiconductors. Additionally, we determined the TECs for cell volume and *c*-lattice parameter as $(3.6 \pm 0.2) \times 10^{-5}$ $K^{-1}$ and $(5.7 \pm 2) \times 10^{-5}$ $K^{-1}$, respectively, which also agree with reported bulk multilayer values (Figure 4b,c).[44,47,56,57] Statistical analysis reveals that we can determine a significant relationship between *c* and the temperature. The small $(01\bar{1}1)$ peak that was detected in sample 2 resulted from a tear that introduced a rolled edge, allowing us to track changes in the *c*-lattice parameter. Only measurements from sample 2, which had the $(01\bar{1}1)$ peak present, were used in the calculation of the out-of-plane TEC value. We note that the change in *c*-lattice parameter was indistinguishable for all measurements across both samples at 18 and 73 °C, followed by expansion with comparable deviation between measurements from 138 to 564 °C which contributed to the trend of increasing statistical deviation with temperature seen in the cell volume calculations.

Figure 4 shows the averages of the measurements at each temperature point with 95% confidence bands. Future measurements can be improved further with experimental techniques such as aberration-corrected STEM and improved detectors by enhancing the resolution and collection efficiency. A summary of TECs for $WSe_2$ compared with these results is given in Table 2, and discrepancies in the reports indicate additional physics that may be captured by the different measurement techniques which will require additional investigations by this field. Previous studies have shown a strong relationship between thermal expansion on and layer thickness.[2] The 4D-STEM method for measuring TECs can be expanded in the future to simultaneously incorporate local thickness measurements by employing the common technique of diffraction intensity for 1-layer, 2-layer, and 3-layer materials.

**Table 2. Comparison of the In-Plane ($\alpha_a$) and Out-of-Plane ($\alpha_c$) Thermal Expansion Coefficients for $WSe_2$**

| sample | $\alpha_a$ ($10^{-6}$ $K^{-1}$) | $\alpha_c$ ($10^{-6}$ $K^{-1}$) | comments |
|---|---|---|---|
| 1 layer[2] | 154 ± 7 | | suspended, plasmon shift |
| 1 layer[3] | 7 ± 1 | | supported, Raman |
| 1 layer[58] | 7.4 | | theoretical, 20 °C |
| 1 layer (this work) | 7.53 | | theoretical, 20 °C |
| nominally 1 layer (this work) | 3.5 ± 0.9 | 57 ± 20 | suspended, polycrystalline, nanodiffraction |
| 2 layer[2] | 42 ± 3 | | suspended, plasmon shift |
| 3 layer[2] | 27 ± 3 | | suspended, plasmon shift |
| bulk[44] | 5.132 | 8.105 | X-ray diffraction (XRD) |
| bulk[47] | 11.08 | 16.72 | powder XRD |
| bulk[59] | 6.8 | 10.6 | powder XRD |
| bulk[56] | 14.45 | 13.74 | powder XRD |
| bulk (this work) | 5.65 | 9.69 | theoretical, 20 °C |

Lattice distortions, specifically strain, were determined from the broadening of the corrected peaks in the radial peak histogram and is measured in terms of the FWHM of the fitted Gaussian using the Halder–Wagner model.[60] The Williamson–Hall plot was used to calculate the apparent microstrain as a function of temperature, which represents quantification of the upper limit of strain in the sample and indicates an overall decrease in the progression of strain versus an increase in temperature (Figure 4d). Scatter in the linear distribution may indicate structural defects. Figure S4 presents the 2D spatial strain profiles near the fracture location in sample 2 at the temperature limits reported here.

The attribution of different multiscale components including heating-related stress relaxation at grain boundaries to the overall TEC is rather complex. According to a previous report,[61] single-crystal samples grown as triangular shapes typically exhibit strain due to differences in the thermal coefficient of expansion between the 2D film and growth substrate. Their report demonstrates that after stress relaxation by transferring from the growth substrate to a secondary substrate, the Raman shift recovered to 250 $cm^{-1}$ and the photoluminescence (PL) recovered to 1.65 eV. The change in PL was significant with an ∼0.07 eV red shift for the strained sample compared to the relaxed sample, while the change in Raman was smaller and on the order of a 1.5 $cm^{-1}$ red shift for the strained sample. However, in our case, where the sample is polycrystalline, we did not observe significant strain in the as-grown sample when comparing its Raman and PL spectra with those of exfoliated single-crystal samples, while the PL slightly blue-shifted by 21 meV after wet transfer (Figure S5, Supporting Information). This near absence of strain in the as-grown samples may be attributed to a stress relaxation mechanism within the polycrystalline lattice at high temperatures and may indeed be incorporated in the lower in-plane TEC values we obtain compared to the exfoliated single crystals of previous reports,[2,3] and thus we note that the TEC reported here is that for the polycrystalline monolayer $WSe_2$.

We have also predicted the thermal expansion coefficients of bulk and monolayer $WSe_2$ using first-principles methods within the quasi-harmonic approximation (QHA). The density functional theory (DFT) optimized lattice parameters at 0 K for bulk are $a = b = 3.3373$ Å and $c = 12.8171$ Å, and for monolayer are $a = b = 3.3244$ Å for monolayer, which is in close agreement with experimental lattice parameters. The thermal expansion coefficient was calculated from the *ab initio* theoretical calculations using seventh-order polynomials of the form

$$\alpha_{a,\mathrm{bulk}} = \frac{1}{a_{\mathrm{bulk}}}\frac{\partial}{\partial T}(a_{\mathrm{bulk}}) = -4.71 \times 10^{-25}T^7 + 1.59 \times 10^{-21}T^6 - 2.03 \times 10^{-18}T^5 + 1.11 \times 10^{-15}T^4 - 1.28 \times 10^{-13}T^3 - 1.23 \times 10^{-10}T^2 + 5.14 \times 10^{-8}T - 3.25 \times 10^{-7} \quad (1a)$$



https://doi.org/10.1021/acsnano.4c02996
ACS Nano 2024, 18, 17725−17734

$$\alpha_{c,\mathrm{bulk}} = \frac{1}{c_{\mathrm{bulk}}}\frac{\partial}{\partial T}(c_{\mathrm{bulk}}) = 1.73 \times 10^{-26}T^7 - 8.32 \times 10^{-23}T^6 + 1.80 \times 10^{-19}T^5 - 2.35 \times 10^{-16}T^4 + 2.07 \times 10^{-13}T^3 - 1.27 \times 10^{-10}T^2 + 5.08 \times 10^{-8}T + 1.92 \times 10^{-6} \quad (1b)$$

$$\alpha_{a,\mathrm{monolayer}} = \frac{1}{a_{\mathrm{monolayer}}}\frac{\partial}{\partial T}(a_{\mathrm{monolayer}}) = -5.07 \times 10^{-25}T^7 + 1.63 \times 10^{-21}T^6 - 1.88 \times 10^{-18}T^5 + 7.73 \times 10^{-16}T^4 + 1.63 \times 10^{-13}T^3 - 2.46 \times 10^{-10}T^2 + 7.72 \times 10^{-8}T - 6.41 \times 10^{-7} \quad (2)$$

where $T$ is in units of Kelvin, as is commonly employed.[62] To gain insight into the asymptotic behavior of thermal expansion, the TECs can also be fit with a single-parameter asymptotic function of the form

$$\alpha_{a,\mathrm{bulk}} = 5.888 \times 10^{-6} - 6.456 \times 10^{-6}(0.990^T) \quad (3a)$$

$$\alpha_{c,\mathrm{bulk}} = 1.198 \times 10^{-5} - 1.006 \times 10^{-5}(0.995^T) \quad (3b)$$

$$\alpha_{a,\mathrm{monolayer}} = 8.057 \times 10^{-6} - 8.850 \times 10^{-6}(0.990^T) \quad (4)$$

where $T$ is in units of Kelvin, although we note that for the monolayer case, the $\alpha_a$ does not approach an asymptote and continues to slightly increase with temperature to 1000 K. The linear thermal expansion coefficients for the in-plane lattice parameter $a$ was $7.53 \times 10^{-6}$ $K^{-1}$ for monolayer $WSe_2$ and $5.65 \times 10^{-6}$ $K^{-1}$ for bulk, suggesting that $\alpha_a$ is higher in monolayer than bulk as reported in ref 2. The out-of-plane thermal expansion coefficient for the $c$-lattice parameter in bulk was calculated to be $9.69 \times 10^{-6}$ $K^{-1}$. These calculated results show good agreement with experiment, although are slightly higher than the in-plane value we obtained and lower than the out-of-plane value. This is likely due, in the case of the in-plane TEC, to stress relaxation mechanisms in the polycrystalline material of this study.

## CONCLUSIONS

We demonstrate a methodology that combines 4D-STEM with advanced postprocessing and computational analysis to determine the local thermal expansion coefficient of a polycrystalline 2D TMD material. Using 4D-STEM to determine thermomechanical properties has the advantage of being a direct measurement on free-standing samples. Robust uncertainty analysis shows that the optimized calibration in the computational method can produce precise localized lattice parameters. Our results confirm the TEC for $WSe_2$ 2D material is within the expected range for industrially relevant semiconductors and agrees closely with the bulk values reported previously, showing promise for industrial integration including remote epitaxy.[63−65] The methodology presented here can be expanded to other 2D materials for the accurate determination of localized TECs without the use of substrates or indirect measurements.

## METHODS

**MOCVD Growth of $WSe_2$ on $SiO_2$/Si.** Layered $WSe_2$ films were grown on 2-inch Si substrates coated with $SiO_2$ (~285 nm) using a vertical cold-wall metal−organic chemical vapor deposition (MOCVD) technique. Tungsten hexacarbonyl [THC, $W(CO)_6$] and diethyl selenide [DESe, $(C_2H_5)_2Se$] were used as transition metal (W) and chalcogen (Se) precursors, respectively. The 2 inch $SiO_2$/Si substrates were loaded on a graphite susceptor in the vertical reactor, heated to 600 °C at 45 °C $min^{-1}$, and preannealed for surface cleaning. The vapor-phase THC and DESe precursors were injected into the MOCVD reactor after reaching the growth temperature. After the growth process, the $WSe_2$ sample was naturally cooled to room temperature and unloaded.

**Transfer of $WSe_2$ Film to TEM Cu Grid.** A wet sample transfer method[66] was used to prepare the samples for 4D-STEM. $WSe_2$ films were transferred via a sacrificial polymer by dipping in a mixture of glycerol and Formvar resin [poly(vinyl formal), CAS# 9003-33-2] solution in chloroform. The sample was dried at a 60° inclination for 30 min. The $SiO_2$/Si was etched with HF acid (1% aqueous) for 20 min following sequential deionized water baths to create a floating film. The free-standing Formvar-coated $WSe_2$ film was then transferred to a QUANTIFOIL holey carbon-supported Cu TEM grid followed by annealing in a vacuum furnace at 50 °C for 10 min to improve adhesion. The sacrificial Formvar film was then removed by submersing the grid in chloroform.

**4D-STEM of $WSe_2$.** Temperature experiments were performed at the National Center for Electron Microscopy at Lawrence Berkeley National Laboratory. 4D-STEM data sets were collected for two samples of $WSe_2$ over the temperature range of 18−564 °C. The TitanX electron microscope in STEM mode equipped with a Gatan Orius 830 CCD camera operating at 60 kV with a Gatan 652 heating holder was used for the experiments. Acquisition of NBED patterns was performed with a 25−200 ms dwell time, a convergence semiangle of 1 mrad, and a 195 mm camera length. Data processing was performed using a suite of custom MATLAB algorithms, including lattice parameter calculation, and py4DSTEM.[48,49]

**Computational Method.** We have utilized the quasi-harmonic approximation (QHA) to calculate the thermal expansion coefficient of bulk and monolayer $WSe_2$ at constant pressure, as implemented in the PHONOPY package.[67] The phononic contribution to the free energy at constant volumes were calculated using phonon density of states and utilized to calculate the Gibbs free energy as a function of temperature. The equation of state was fitted for 7 different volumetric points (−3 to 3% strain with a step size of 1%), for which structures were relaxed using first-principles calculation within the density functional theory (DFT) using Quantum ESPRESSO.[68] A plane-wave basis set with an energy cutoff of 1088 eV was used for expressing the wave function. We used the Perdew−Burke−Ernzerhof (PBE) generalized gradient approximation,[69] with semiempirical Grimme-D2 van der Waals correction[70] to the total energy for bulk, which is common practice in layered systems.[71−73] We used Optimized Norm-Conserving Vanderbilt pseudopotentials[74] from the Pseudodojo set.[75] The Brillouin zone was sampled by a half-shifted 6 × 6 × 2 (for bulk) and 12 × 12 × 1 (for monolayer) Monkhorst−Pack $k$-point mesh, and the position of atoms in the structure was optimized until the forces on every atom were ≤0.0001 eV/Å. For the monolayer calculation, a vacuum space of 15 Å was used to reduce the spurious periodicity. Phonon calculations to predict the free energy contribution were performed by using the supercell approach. All structures at different volume force constants were calculated for a 3 × 3 × 1 supercell using PHONOPY.[67]

## ASSOCIATED CONTENT

### Supporting Information

The Supporting Information is available free of charge at https://pubs.acs.org/doi/10.1021/acsnano.4c02996.



https://doi.org/10.1021/acsnano.4c02996
ACS Nano 2024, 18, 17725−17734

Additional experimental and computational details, including patterned-probe template and elliptical corrections, orientation maps, and strain maps (PDF)

## AUTHOR INFORMATION


### Corresponding Author

**Michael T. Pettes** − *Center for Integrated Nanotechnologies (CINT), Materials Physics and Applications Division, Los Alamos National Laboratory, Los Alamos, New Mexico 87545, United States;* orcid.org/0000-0001-6862-6841; Email: pettesmt@lanl.gov.

### Authors

**Theresa M. Kucinski** − *Center for Integrated Nanotechnologies (CINT), Materials Physics and Applications Division, Los Alamos National Laboratory, Los Alamos, New Mexico 87545, United States; Nuclear Materials Science Group (MST-16), Materials and Technology Division, Los Alamos National Laboratory, Los Alamos, New Mexico 87545, United States*

**Rohan Dhall** − *National Center for Electron Microscopy (NCEM), The Molecular Foundry, Lawrence Berkeley National Laboratory, Berkeley, California 94720, United States*

**Benjamin H. Savitzky** − *National Center for Electron Microscopy (NCEM), The Molecular Foundry, Lawrence Berkeley National Laboratory, Berkeley, California 94720, United States*

**Colin Ophus** − *National Center for Electron Microscopy (NCEM), The Molecular Foundry, Lawrence Berkeley National Laboratory, Berkeley, California 94720, United States*

**Rijan Karkee** − *Center for Integrated Nanotechnologies (CINT), Materials Physics and Applications Division, Los Alamos National Laboratory, Los Alamos, New Mexico 87545, United States;* orcid.org/0000-0003-0124-5213

**Avanish Mishra** − *Physics and Chemistry of Materials Group (T-1), Theoretical Division, Los Alamos National Laboratory, Los Alamos, New Mexico 87545, United States*

**Enkeleda Dervishi** − *Electrochemistry and Corrosion Team, Sigma Division, Los Alamos National Laboratory, Los Alamos, New Mexico 87545, United States*

**Jung Hoon Kang** − *Department of Electrical & Computer Engineering, Seoul National University, Seoul 08826, Republic of Korea*

**Chul-Ho Lee** − *Department of Electrical & Computer Engineering, Seoul National University, Seoul 08826, Republic of Korea;* orcid.org/0000-0003-1570-8688

**Jinkyoung Yoo** − *Center for Integrated Nanotechnologies (CINT), Materials Physics and Applications Division, Los Alamos National Laboratory, Los Alamos, New Mexico 87545, United States;* orcid.org/0000-0002-9578-6979

Complete contact information is available at: https://pubs.acs.org/10.1021/acsnano.4c02996


### Notes

The authors declare no competing financial interest.

## ACKNOWLEDGMENTS

This work was supported by the Laboratory Directed Research and Development program of Los Alamos National Laboratory under project numbers 20230014DR, 20220485MFR, and 20190516ECR, and National Security Education Center under project numbers IMS RR19PETT, IMS RR21PETT, and ISTI IP2104MP. Work at the Molecular Foundry was supported by the Office of Science, Office of Basic Energy Sciences, of the U.S. Department of Energy under Contract no. DE-AC02-05CH11231. C.O. acknowledges additional support from the Department of Energy Early Career Research Award program. C.-H.L. acknowledges the support by the National R&D Program through the National Research Foundation of Korea (NRF) funded by the Ministry of Science and ICT (2023R1A2C3005923 and 2020M3D1A1110548). This work was performed in part at the Center for Integrated Nanotechnologies, an Office of Science User Facility operated for the U.S. Department of Energy (DOE) Office of Science. Los Alamos National Laboratory, an affirmative action equal opportunity employer, is managed by Triad National Security, LLC for the U.S. Department of Energy's NNSA, under contract 89233218CNA000001.

## REFERENCES


(1) Gargini, P. *International Roadmap for Devices and Systems (IRDS) 2023 Update*, The Institute of Electrical and Electronics Engineers, Incorporated, 2023. https://irds.ieee.org/editions/2023.

(2) Hu, X.; Yasaei, P.; Jokisaari, J.; Öğüt, S.; Salehi-Khojin, A.; Klie, R. F. Mapping thermal expansion coefficients in freestanding 2D materials at the nanometer scale. *Phys. Rev. Lett.* **2018**, *120*, No. 055902.

(3) Zhong, Y.; Zhang, L.; Park, J.-H.; Cruz, S.; Li, L.; Guo, L.; Kong, J.; Wang, E. N. A unified approach and descriptor for the thermal expansion of two-dimensional transition metal dichalcogenide monolayers. *Sci. Adv.* **2022**, *8*, No. eabo3783.

(4) Shrivastava, M.; Ramgopal Rao, V. A roadmap for disruptive applications and heterogeneous integration using two-dimensional materials: State-of-the-art and technological challenges. *Nano Lett.* **2021**, *21*, 6359−6381.

(5) Wu, F.; Tian, H.; Shen, Y.; Zhu, Z.-Q.; Liu, Y.; Hirtz, T.; Wu, R.; Gou, G.; Qiao, Y.; Yang, Y.; Xing, C.-Y.; Zhang, G.; Ren, T.-L. High thermal conductivity 2D materials: From theory and engineering to applications. *Adv. Mater. Interfaces* **2022**, *9*, No. 2200409.

(6) Wu, W.; Dass, C. K.; Hendrickson, J. R.; Montaño, R. D.; Fischer, R. E.; Zhang, X.; Choudhury, T. H.; Redwing, J. M.; Wang, Y.; Pettes, M. T. Locally defined quantum emission from epitaxial few-layer tungsten diselenide. *Appl. Phys. Lett.* **2019**, *114*, No. 213102.

(7) Wang, X.; Pettes, M. T.; Wang, Y.; Zhu, J.-X.; Dhall, R.; Song, C.; Jones, A. C.; Ciston, J.; Yoo, J. Enhanced exciton-to-trion conversion by proton irradiation of atomically thin $WS_2$. *Nano Lett.* **2023**, *23*, 3754−3761.

(8) Li, X.; Jones, A. C.; Choi, J.; Zhao, H.; Chandrasekaran, V.; Pettes, M. T.; Piryatinski, A.; Tschudin, M. A.; Reiser, P.; Broadway, D. A.; Maletinsky, P.; Sinitsyn, N.; Crooker, S. A.; Htoon, H. Proximity-induced chiral quantum light generation in strain-engineered $WSe_2/NiPS_3$ heterostructures. *Nat. Mater.* **2023**, *22*, 1311−1316.

(9) Mak, K. F.; Lee, C.; Hone, J.; Shan, J.; Heinz, T. F. Atomically thin $MoS_2$: A new direct-gap semiconductor. *Phys. Rev. Lett.* **2010**, *105*, No. 136805.

(10) Radisavljevic, B.; Whitwick, M. B.; Kis, A. Integrated circuits and logic operations based on single-layer $MoS_2$. *ACS Nano* **2011**, *5*, 9934−9938.

(11) Rosenberger, M. R.; Dass, C. K.; Chuang, H.-J.; Sivaram, S. V.; McCreary, K. M.; Hendrickson, J. R.; Jonker, B. T. Quantum calligraphy: Writing single-photon emitters in a two-dimensional materials platform. *ACS Nano* **2019**, *13*, 904−912.

(12) Dai, Z.; Liu, L.; Zhang, Z. Strain engineering of 2D materials: Issues and opportunities at the interface. *Adv. Mater.* **2019**, *31*, No. 1805417.

(13) Iannaccone, G.; Bonaccorso, F.; Colombo, L.; Fiori, G. Quantum engineering of transistors based on 2D materials heterostructures. *Nat. Nanotechnol.* **2018**, *13*, 183−191.
(14) Ge, R.; Wu, X.; Kim, M.; Shi, J.; Sonde, S.; Tao, L.; Zhang, Y.; Lee, J. C.; Akinwande, D. Atomristor: Nonvolatile resistance switching in atomic sheets of transition metal dichalcogenides. *Nano Lett.* **2018**, *18*, 434−441.
(15) Ghosh Dastidar, M.; Thekkooden, I.; Nayak, P. K.; Bhallamudi, V. P. Quantum emitters and detectors based on 2D van der Waals materials. *Nanoscale* **2022**, *14*, 5289−5313.
(16) Yu, J.; Hossain, M. A.; Kim, S.; Ferrari, P. F.; Huang, S.; Zhang, Y.; Kim, H.; Michel, D. A.; van der Zande, A. M. Mechanically sensing and tailoring electronic properties in two-dimensional atomic membranes. *Curr. Opin. Solid State Mater. Sci.* **2021**, *25*, No. 100900.
(17) Wu, W.; Morales-Acosta, M. D.; Wang, Y.; Pettes, M. T. Isotope effect in bilayer $WSe_2$. *Nano Lett.* **2019**, *19*, 1527−1533.
(18) Xia, F.; Wang, H.; Xiao, D.; Dubey, M.; Ramasubramaniam, A. Two-dimensional material nanophotonics. *Nat. Photon.* **2014**, *8*, 899−907.
(19) Chakraborty, C.; Vamivakas, N. A.; Englund, D. Advances in quantum light emission from 2D materials. *Nanophotonics* **2019**, *8*, 2017−2032.
(20) Liu, X.; Hersam, M. C. 2D materials for quantum information science. *Nat. Rev. Mater.* **2019**, *4*, 669−684.
(21) Cheng, Q.; Pang, J.; Sun, D.; Wang, J.; Zhang, S.; Liu, F.; Chen, Y.; Yang, R.; Liang, N.; Lu, X.; et al. $WSe_2$ 2D p-type semiconductor-based electronic devices for information technology: Design, preparation, and applications. *InfoMat* **2020**, *2*, 656−697.
(22) Liu, C.; Chen, H.; Wang, S.; Liu, Q.; Jiang, Y.-G.; Zhang, D. W.; Liu, M.; Zhou, P. Two-dimensional materials for next-generation computing technologies. *Nat. Nanotechnol.* **2020**, *15*, 545−557.
(23) Mondal, N.; Azam, N.; Gartstein, Y. N.; Mahjouri-Samani, M.; Malko, A. V. Photoexcitation dynamics and long-lived excitons in strain-engineered transition metal dichalcogenides. *Adv. Mater.* **2022**, *34*, No. 2110568.
(24) Rai, S.; Singh, V. K.; Pendurthi, R.; Nasr, J. R.; Das, S.; Srivastava, A. Unveiling the electrical and photo-physical properties of intrinsic n-type 2D $WSe_2$ for high performance field-effect transistors. *J. Appl. Phys.* **2022**, *131*, No. 094301.
(25) Huang, Y.; Gu, Y.; Mohan, S.; Dolocan, A.; Ignacio, N. D.; Kutagulla, S.; Matthews, K.; Londoño-Calderon, A.; Chang, Y.-F.; Chen, Y.-C.; Warner, J. H.; Pettes, M. T.; Lee, J. C.; Akinwande, D. Reliability improvement and effective switching layer model of thin-film $MoS_2$ memristors. *Adv. Funct. Mater.* **2023**, *34* (15), No. 2214250.
(26) Yang, J. A.; Bennett, R. K. A.; Hoang, L.; Zhang, Z.; Thompson, K. J.; Michail, A.; Parthenios, J.; Papagelis, K.; Mannix, A. J.; Pop, E.Biaxial tensile strain enhances electron mobility of monolayer transition metal dichalcogenides *arXiv* 2023, 2309.10939 [cond-mat.mes-hall]. DOI: 10.48550/arXiv.2309.10939.
(27) Datye, I. M.; Daus, A.; Grady, R. W.; Brenner, K.; Vaziri, S.; Pop, E. Strain-enhanced mobility of monolayer $MoS_2$. *Nano Lett.* **2022**, *22*, 8052−8059.
(28) Wu, W.; Wang, J.; Ercius, P.; Wright, N. C.; Leppert-Simenauer, D. M.; Burke, R. A.; Dubey, M.; Dongare, A. M.; Pettes, M. T. Giant mechano-optoelectronic effect in an atomically thin semiconductor. *Nano Lett.* **2018**, *18*, 2351−2357.
(29) Steward, E. G.; Cook, B. P.; Kellett, E. A. Dependence on temperature of the interlayer spacing in carbons of different graphitic perfection. *Nature* **1960**, *187*, 1015−1016.
(30) Lau, C. N.; Bao, W.; Velasco, J. Properties of suspended graphene membranes. *Mater. Today* **2012**, *15*, 238−245.
(31) Lin, Z.; Liu, W.; Tian, S.; Zhu, K.; Huang, Y.; Yang, Y. Thermal expansion coefficient of few-layer $MoS_2$ studied by temperature-dependent Raman spectroscopy. *Sci. Rep.* **2021**, *11*, No. 7037.
(32) Lin, Y.-C.; Jariwala, B.; Bersch, B. M.; Xu, K.; Nie, Y.; Wang, B.; Eichfeld, S. M.; Zhang, X.; Choudhury, T. H.; Pan, Y.; Addou, R.; Smyth, C. M.; Li, J.; Zhang, K.; Haque, M. A.; Fölsch, S.; Feenstra, R. M.; Wallace, R. M.; Cho, K.; Fullerton-Shirey, S. K.; Redwing, J. M.; Robinson, J. A. Realizing large-scale, electronic-grade two-dimensional semiconductors. *ACS Nano* **2018**, *12*, 965−975.
(33) Eichfeld, S. M.; Hossain, L.; Lin, Y.-C.; Piasecki, A. F.; Kupp, B.; Birdwell, A. G.; Burke, R. A.; Lu, N.; Peng, X.; Li, J.; Azcatl, A.; McDonnell, S.; Wallace, R. M.; Kim, M. J.; Mayer, T. S.; Redwing, J. M.; Robinson, J. A. Highly scalable, atomically thin $WSe_2$ grown via metal−organic chemical vapor deposition. *ACS Nano* **2015**, *9*, 2080−2087.
(34) Chubarov, M.; Choudhury, T. H.; Hickey, D. R.; Bachu, S.; Zhang, T.; Sebastian, A.; Bansal, A.; Zhu, H.; Trainor, N.; Das, S.; Terrones, M.; Alem, N.; Redwing, J. M. Wafer-scale epitaxial growth of unidirectional $WS_2$ monolayers on sapphire. *ACS Nano* **2021**, *15*, 2532−2541.
(35) Lee, D. H.; Sim, Y.; Wang, J.; Kwon, S.-Y. Metal-organic chemical vapor deposition of 2D van der Waals materials—The challenges and the extensive future opportunities. *APL Mater.* **2020**, *8*, No. 030901.
(36) Xu, X.; Guo, T.; Kim, H.; Hota, M. K.; Alsaadi, R. S.; Lanza, M.; Zhang, X.; Alshareef, H. N. Growth of 2D materials at the wafer scale. *Adv. Mater.* **2022**, *34*, No. 2108258.
(37) Kang, T.; Tang, T. W.; Pan, B.; Liu, H.; Zhang, K.; Luo, Z. Strategies for controlled growth of transition metal dichalcogenides by chemical vapor deposition for integrated electronics. *ACS Mater. Au* **2022**, *2*, 665−685.
(38) Lei, L.; Lun, Y.; Cao, F.; Meng, L.; Xing, S.; Guo, J.; Dong, H.; Gu, S.; Xu, K.; Hussain, S.; et al. Size-dependent strain-engineered nanostructures in $MoS_2$ monolayer investigated by atomic force microscopy. *Nanotechnology* **2021**, *32*, No. 465703.
(39) Zhang, L.; Wang, H.; Zong, X.; Zhou, Y.; Wang, T.; Wang, L.; Chen, X. Probing interlayer shear thermal deformation in atomically-thin van der Waals layered materials. *Nat. Commun.* **2022**, *13*, No. 3996.
(40) Kaya, O.; Donmezer, N. Investigation of the thermal transport properties across van der Waals interfaces of 2D materials. *IEEE Trans. Nanotechnol.* **2022**, *21*, 592−597.
(41) Huang, X.; Gao, Y.; Yang, T.; Ren, W.; Cheng, H.-M.; Lai, T. Quantitative analysis of temperature dependence of Raman shift of monolayer $WS_2$. *Sci. Rep.* **2016**, *6*, No. 32236.
(42) Chaikasetsin, S.; Kodama, T.; Bae, K.; Jung, J. Y.; Shin, J.; Lee, B. C.; Kim, B. S. Y.; Seo, J.; Sim, U.; Prinz, F. B.; Goodson, K. E.; Park, W. Thermal expansion characterization of thin films using harmonic Joule heating combined with atomic force microscopy. *Appl. Phys. Lett.* **2021**, *118*, No. 194101, DOI: 10.1063/5.0049160.
(43) Zhang, D.; Wu, Y.-C.; Yang, M.; Liu, X.; Coileáin, C. Ó.; Xu, H.; Abid, M.; Abid, M.; Wang, J.-J.; Shvets, I. V.; Liu, H.; Wang, Z.; Yin, H.; Liu, H.; Chun, B. S.; Zhang, X.; Wu, H.-C. Probing thermal expansion coefficients of monolayers using surface enhanced Raman scattering. *RSC Adv.* **2016**, *6*, 99053−99059.
(44) Mathew, S.; Abraham, A. R.; Chintalapati, S.; Sarkar, S.; Joseph, B.; Venkatesan, T. Temperature dependent structural evolution of $WSe_2$: A synchrotron X-ray diffraction study. *Condens. Matter* **2020**, *5*, 76.
(45) Paul, S.; Torsi, R.; Robinson, J. A.; Momeni, K. Effect of the substrate on $MoS_2$ monolayer morphology: An integrated computational and experimental study. *ACS Appl. Mater. Interfaces* **2022**, *14*, 18835−18844.
(46) Morell, N.; Reserbat-Plantey, A.; Tsioutsios, I.; Schädler, K. G.; Dubin, F.; Koppens, F. H. L.; Bachtold, A. High quality factor mechanical resonators based on $WSe_2$ monolayers. *Nano Lett.* **2016**, *16*, 5102−5108.
(47) El-Mahalawy, S. H.; Evans, B. L. The thermal expansion of 2H-$MoS_2$, 2H-$MoSe_2$ and 2H-$WSe_2$ between 20 and 800 °C. *J. Appl. Crystallogr.* **1976**, *9*, 403−406.
(48) Savitzky, B. H.; Zeltmann, S. E.; Hughes, L. A.; Brown, H. G.; Zhao, S.; Pelz, P. M.; Pekin, T. C.; Barnard, E. S.; Donohue, J.; DaCosta, L. R.; Kennedy, E.; Xie, Y.; Janish, M. T.; Schneider, M. M.; Herring, P.; Gopal, C.; Anapolsky, A.; Dhall, R.; Bustillo, K. C.; Ercius, P.; Scott, M. C.; Ciston, J.; Minor, A. M.; Ophus, C. py4DSTEM: A software package for four-dimensional scanning

transmission electron microscopy data analysis. *Microsc. Microanal.* **2021**, *27*, 712−743.
(49) Ophus, C.; Zeltmann, S. E.; Bruefach, A.; Rakowski, A.; Savitzky, B. H.; Minor, A. M.; Scott, M. C. Automated crystal orientation mapping in py4DSTEM using sparse correlation matching. *Microsc. Microanal.* **2022**, *28*, 390−403.
(50) Ophus, C. Four-dimensional scanning transmission electron microscopy (4D-STEM): From scanning nanodiffraction to ptychography and beyond. *Microsc. Microanal.* **2019**, *25*, 563−582.
(51) Londoño-Calderon, A.; Williams, D. J.; Schneider, M. M.; Savitzky, B. H.; Ophus, C.; Pettes, M. T. Local lattice deformation of tellurene grain boundaries by four-dimensional electron microscopy. *J. Phys. Chem. C* **2021**, *125*, 3396−3405.
(52) Zeltmann, S. E.; Müller, A.; Bustillo, K. C.; Savitzky, B.; Hughes, L.; Minor, A. M.; Ophus, C. Patterned probes for high precision 4D-STEM Bragg measurements. *Ultramicroscopy* **2020**, *209*, No. 112890.
(53) Mahr, C.; Müller-Caspary, K.; Ritz, R.; Simson, M.; Grieb, T.; Schowalter, M.; Krause, F. F.; Lackmann, A.; Soltau, H.; Wittstock, A.; Rosenauer, A. Influence of distortions of recorded diffraction patterns on strain analysis by nano-beam electron diffraction. *Ultramicroscopy* **2019**, *196*, 74−82.
(54) Savitzky, B. H.; Hughes, L.; Bustillo, K. C.; Deng, H. D.; Jin, N. L.; Lomeli, E. G.; Chueh, W. C.; Herring, P.; Minor, A.; Ophus, C. py4DSTEM: Open source software for 4D-STEM data analysis. *Microsc. Microanal.* **2019**, *25*, 124−125.
(55) Wong-Ng, W.; McMurdie, H. F.; Paretzkin, B.; Zhang, Y.; Davis, K. L.; Hubbard, C. R.; Dragoo, A. L.; Stewart, J. M. Reference x-ray diffraction powder patterns of fifteen ceramic phases. *Powder Diffr.* **1987**, *2*, 257−265.
(56) Murray, R.; Evans, B. The thermal expansion of 2H-$MoS_2$ and 2H-$WSe_2$ between 10 and 320 K. *J. Appl. Crystallogr.* **1979**, *12*, 312−315.
(57) Bhatt, S. V.; Deshpande, M. P.; Sathe, V.; Rao, R.; Chaki, S. H. Raman spectroscopic investigations on transition-metal dichalcogenides $MX_2$ (M = Mo, W; X = S, Se) at high pressures and low temperature. *J. Raman Spectrosc.* **2014**, *45*, 971−979.
(58) Çakır, D.; Peeters, F. M.; Sevik, C. Mechanical and thermal properties of *h*-$MX_2$ (M = Cr, Mo, W; X = O, S, Se, Te) monolayers: A comparative study. *Appl. Phys. Lett.* **2014**, *104*, No. 203110.
(59) Brixner, L. H. X-ray study and thermoelectric properties of the $W_xTa_{1-x}Se_2$ system. *J. Electrochem. Soc.* **1963**, *110*, 289−293.
(60) Londoño-Calderon, A.; Williams, D. J.; Ophus, C.; Pettes, M. T. 1D to 2D transition in tellurium observed by 4D electron microscopy. *Small* **2020**, *16*, No. 2005447.
(61) Ahn, G. H.; Amani, M.; Rasool, H.; Lien, D.-H.; Mastandrea, J. P.; Ager Iii, J. W.; Dubey, M.; Chrzan, D. C.; Minor, A. M.; Javey, A. Strain-engineered growth of two-dimensional materials. *Nat. Commun.* **2017**, *8*, No. 608.
(62) Kirby, R. K. Platinum—A thermal expansion reference material. *Int. J. Thermophys.* **1991**, *12*, 679−685.
(63) Bae, S.-H.; Kum, H.; Kong, W.; Kim, Y.; Choi, C.; Lee, B.; Lin, P.; Park, Y.; Kim, J. Integration of bulk materials with two-dimensional materials for physical coupling and applications. *Nat. Mater.* **2019**, *18*, 550−560.
(64) Wang, X.; Kaufmann, R.; Jones, A. C.; Chen, R.; Ahmed, T.; Pettes, M. T.; Kotula, P. G.; Bilgin, I.; Wang, Y.; Kar, S.; Yoo, J. Evidence of hexagonal germanium grains on annealed monolayer $MoS_2$. *Mater. Today Adv.* **2023**, *19*, No. 100401.
(65) Liang, D.; Wei, T.; Wang, J.; Li, J. Quasi van der Waals epitaxy nitride materials and devices on two dimension materials. *Nano Energy* **2020**, *69*, No. 104463.
(66) Auchter, E.; Marquez, J.; Yarbro, S. L.; Dervishi, E. A facile alternative technique for large-area graphene transfer via sacrificial polymer. *AIP Adv.* **2017**, *7*, No. 125306.
(67) Togo, A.; Tanaka, I. First principles phonon calculations in materials science. *Scripta Mater.* **2015**, *108*, 1−5.
(68) Giannozzi, P.; Andreussi, O.; Brumme, T.; Bunau, O.; Nardelli, M. B.; Calandra, M.; Car, R.; Cavazzoni, C.; Ceresoli, D.; Cococcioni, M.; Colonna, N.; Carnimeo, I.; Dal Corso, A.; de Gironcoli, S.; Delugas, P.; DiStasio, R. A.; Ferretti, A.; Floris, A.; Fratesi, G.; Fugallo, G.; Gebauer, R.; Gerstmann, U.; Giustino, F.; Gorni, T.; Jia, J.; Kawamura, M.; Ko, H. Y.; Kokalj, A.; Kucukbenli, E.; Lazzeri, M.; Marsili, M.; Marzari, N.; Mauri, F.; Nguyen, N. L.; Nguyen, H. V.; Otero-de-la-Roza, A.; Paulatto, L.; Ponce, S.; Rocca, D.; Sabatini, R.; Santra, B.; Schlipf, M.; Seitsonen, A. P.; Smogunov, A.; Timrov, I.; Thonhauser, T.; Umari, P.; Vast, N.; Wu, X.; Baroni, S. Advanced capabilities for materials modelling with QUANTUM ESPRESSO. *J. Phys.: Condens. Matter* **2017**, *29*, No. 465901.
(69) Perdew, J. P.; Burke, K.; Ernzerhof, M. Generalized gradient approximation made simple. *Phys. Rev. Lett.* **1996**, *77*, 3865−3868.
(70) Grimme, S. Semiempirical GGA-type density functional constructed with a long-range dispersion correction. *J. Comput. Chem.* **2006**, *27*, 1787−1799.
(71) Karkee, R.; Guerrero, E.; Strubbe, D. A. Enhanced interlayer interactions in Ni-doped $MoS_2$, and structural and electronic signatures of doping site. *Phys. Rev. Materials* **2021**, *5*, No. 074006.
(72) Park, J. B.; Wu, W.; Wu, J. Y.; Karkee, R.; Kucinski, T. M.; Bustillo, K. C.; Schneider, M. M.; Strubbe, D. A.; Ophus, C. L.; Pettes, M. T. Carrier type switching in bismuth telluride nanoribbons through in-situ organic molecule coating. *Nano Lett.* **2023**, *23*, 11395−11401.
(73) Liu, J.; Shen, T.; Ren, J.-C.; Li, S.; Liu, W. Role of van der Waals interactions on the binding energies of 2D transition-metal dichalcogenides. *Appl. Surf. Sci.* **2023**, *608*, No. 155163.
(74) Hamann, D. R. Optimized norm-conserving Vanderbilt pseudopotentials. *Phys. Rev. B* **2013**, *88*, No. 085117.
(75) http://www.pseudo-dojo.org/.


https://doi.org/10.1021/acsnano.4c02996
*ACS Nano* 2024, 18, 17725−17734